Microwave-assisted Synthesis of Greigite Fe_3S_4 nanosheets wrapped in an rGO Matrix as anode material for Sodium-ion batteries

Ikhwan Choi, Bolin Liu, Youqi Zhu and Chuanbao Cao *

School of Materials Science and Engineering, Beijing Institute of Technology, Beijing, China

*Corresponding author e-mail: cbcao@bit.edu.cn

Abstract. Greigite (Fe_3S_4), which have ferromagnetic in inverse thiospinel (AB_2S_4), is widely researched to use an adsorbent and biomedical field because non-toxicity and abundant in nature. Iron-based materials are known to have a high theoretical capacity because of their multivalent state including redox pairs, but still suffer from collapse and aggregate during the charge/discharge process. Here, the synthesized Fe_3S_4 nanosheet structure materials wrapped with reduced graphene oxide (Fe_3S_4NSs@rGO) were used as an anode electrode material for sodium-ion batteries (SIBs). The nano-sheet structure facilitates ion diffusion through expanded surface area, and rGO can effectively improve electrochemical conductivity and structure stability. As-prepared Fe_3S_4NSs@rGO were used as a host material to insert Na-ion via a conversion process, and the stabilized structure maintains the high capacity and long cycle performance. Thus, the Fe_3S_4NSs@rGO deliver a reversible capacity of 950 mAh g^{-1} after 200 cycles at a current density of 1A g^{-1} and 524 mAh g^{-1} after 400 cycles at a current density of 2A g^{-1}, which is much higher than reported materials.

1. Introduction

Research on renewable energy technologies has been continually developed in response to worries about fossil fuels and environmental problems, which are restricted in their availability. Many new alternative energy production technologies, such as, nuclear power, hydroelectricity, and solar power, are being introduced into the marketplace. Additionally, research on energy conversion devices for effectively storing power generated as a result of technical advancements is ongoing. [1-5] The battery industry, which was founded years ago on the findings of Professor John Goodenough and his team of lithium-ion battery researchers, has been able to get one step closer to achieving a clean energy future that is reliable and efficient by collaborating with smart grids. [6]

Sodium metal, the world's fourth-largest resource under the surface of the earth, has the potential to be used in a next-generation battery. Li^+ and Na^+ have similar electrochemical and chemical properties. In terms of the Standard Hydrogen Electrode (SHE), there is only a small gap of about 300 mV; Na (-2.71V vs SHE), Li (-3.04V vs SHE). [7] High-power performance, low-cost, ease of demand and supply, adaptability to operate in a variety of climatic conditions, and the possibility of free recycling in the face of environmental pollution and ecological influences are all factors that contribute to the compatibility of both sodium-ion batteries and energy storage system (ESS) industries. [8-10] The kinetics of Na^+ is related to the rate performance of the SIBs, which is defined by ion diffusion and electron conductivity. [11, 12] In light of the critical role the anode material plays in sodium energy storage performance, much effort must be expended to achieve outstanding reversibility, sodium dynamics, and a large intrinsic capacity.[13]

Iron sulfide is unique among Transition metal chalcogens (TMCs) in terms of its cheap price, abundant reserves, and lack of toxicity. Numerous investigations have been conducted to determine the electrochemical characteristics and performance of FeS and FeS_2. [14-17] However, electrochemical studies into Fe_3S_4 are inadequate. In recent years, the nanostructure design has been widely investigated as an effective strategy to solve poor capacity retention and cycling problems by shortening the diffusion path and allowing access to electrolytes with a larger surface area. [18-20] Qingjie Zhang et al., obtained nanocrystal Fe_3S_4 anode materials which have a specific capacity of 548 mAh g^{-1} at 0.2 A g^{-1} via solvothermal synthesis method. [21] However, the capacity performance of nanocrystal Fe_3S_4 needs further develop.

Herein, A low-cost, high-performance anode material is obtained through the synthesis of an Fe_3S_4 composite. Reduced graphene oxide (rGO) is widely used in many studies as a promising compound in SIBs to reinforce electrochemical and cyclic performances. [22-24] When the rGO is doped onto the anode material, the original structure of the material is still maintained and the rGO matrix prevents volume expansion during charge and discharge process, resulting in superior storage dynamics. [25] There are no report on the electrochemical

* Corresponding author: cbcao@bit.edu.cn

performance studies of the sodium-ion battery using the Fe_3S_4 nanosheets structure with rGO composite as the anode material. A Fe_3S_4NSs@rGO compound was obtained by microwave-assisted synthesis. Through simple microwave-assisted synthesize, a long reaction time of 10 hours or more, which requires a conventional hydrothermal method, was drastically reduced to within 10 minutes. The Fe_3S_4NSs@rGO composites deliver a capacity of 950 mAh g^{-1} even after 1A g^{-1}, 200 cycles at a wide operating voltage of 0−3V and were able to reach a higher capacity of 524 mAh g^{-1} compared to the existing discharge capacity of Fe_3S_4NSs of 365.8 mAh g^{-1}.

2. Experimental

2.1 Preparation of Fe_3S_4NSs and Fe_3S_4NSs@rGO composites

The reagent used in the experiment is analytical grade, and no further purification was performed during the experiment. Graphene oxide (GO) powders were synthesized by a modified Hummers process by coating natural graphite flake. [26] 0.05g of GO powder was dissolved in 10ml ethylene glycol solvent and stirred for 30 minutes under ultrasonic conditions. Combine 16mmol of $FeCl_3$ and 3mmol of thiourea in an ethylene glycol solvent and agitate until the solution turns transparent yellow. After mixing GO with the solution, agitate for another 10 minutes and heat at 155 °C for 9 minutes in a microwave assisted heating system (MARS 6CEM Corporation, USA). The microwave has been set to 500W. The sediment formed during the heating process was washed several times with deionized water and ethanol through a centrifuge (7500 rpm, 3 min), and then obtained The Fe_3S_4@NSs composites through evaporating residual ethanol. The Fe_3S_4@NSs compound is synthesized in the same method without adding GO in the process.

2.2 Characterization.

The crystal structure of Fe_3S_4NSs@rGO was characterized by the X-ray diffractometer (XRD) of Bruker D8 and proceeded at a scan rate of 5° min^{-1}. To examine the surface elemental and valence state distribution of Fe_3S_4NSs@rGO, X-ray photoelectron spectroscopy (XPS) was conducted using the PHI Quantera model. The structures and sizes of samples were examined using a scanning electron microscope (SEM, Hitachi S-4800). EDAX PW9900 energy dispersive spectrometry (EDS) was examined to analyze the distributions of Fe, S, and C elements in Fe_3S_4NSs@rGO. The morphologies of prepared Fe_3S_4NSs@rGO were examined using JEM-2100F TEM equipment.

2.3 Electrochemical Measurements.

The electrochemical properties of the prepared sample were irradiated through coin-type CR2016 half-cells. As-prepared product was mixed in an 8:1:1 weight ratio with Fe_3S_4NSs@rGO, super p conductive addictive and poly(vinylidene fluoride) binder, and N-methyl-2-pyrrolidone (NMP) was used as a solvent. Electrode was manufactured through a slurry coating process, Cu-foil was used as the current collector. It was dried in an oven at 80°C for 24h to eliminate the residual solvent. The amount of active material coated on Cu-foil was ~1.3 mg. The dried electrodes were sliced into disks measuring 1.1 cm. Sodium metal was used as a counter electrode, and the electrolyte was about 0.3mL of prepared $NaPF_6$ (Aladdin≥ 99.99%) in DEC/EC with a molar ratio of 1:1. The separator was made of glass fiber (Whatman, Grade GF/D), and the coin cell was assembled in an Ar-filled glove box with less than 1 ppm of water and oxygen content. Galvanostatic measurements were performed using a CT2001A Land battery measuring instrument within a voltage window of 0–3 V and at various current densities. On a CHI 660E electrochemical workstation, cyclic voltammetry (CV) was performed at room temperature. Through the same process, Fe_3S_4NSs also tested electrochemical measurements.

3. Results and Discussion

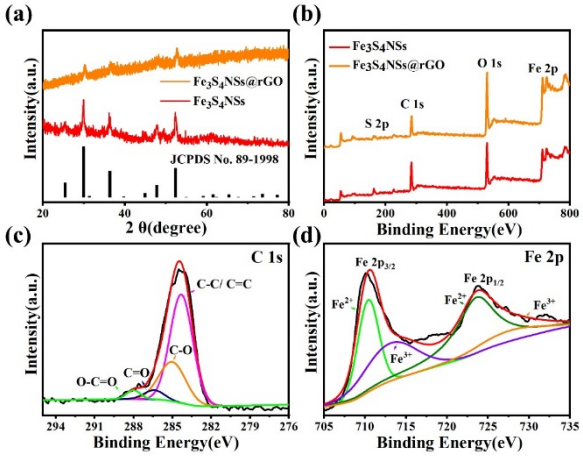

Figure 1. (a) XRD patterns of the Fe_3S_4NSs and Fe_3S_4NSs@rGO composites. (b) Total XPS spectra of the Fe_3S_4NSs and Fe_3S_4NSs@rGO composites. (c-d) High-resolution spectrum of C 1s and Fe 2p.

In this study, thiourea interacts stable with Fe^{2+} to provide sulfur and regulate its structure. The Fe_3S_4 nanosheet structure was prepared through microwave-assisted method. The crystal structure of Fe_3S_4NSs and Fe_3S_4NSs@rGO were characterized as shown Figure 1a. The strong peaks at 29.94°, 36.34° and 52.3° can be attributed Fe_3S_4 cubic phase (JCPDS No. 89-1998) with the face-centered cubic unit composed of 24 iron atoms and 32 sulfur atoms and small crystal sizes can be identified through the presence of broad diffraction peaks. There is no difference between Fe_3S_4NSs and Fe_3S_4NSs@rGO peaks, indicating that the insertion of rGO has no effect on the structure of Fe_3S_4.

Figure 1b-d illustrate the XPS analysis to validate the valence state and element composition of the Fe_3S_4NSs@rGO composites. In Figure 1b, C, O, Fe, and S elements are detected in both spectrums of the Fe_3S_4NSs and Fe_3S_4NSs@rGO. At presented in Figure 1c, C 1s spectrum can be deconvolved into four peaks of 288, 286.4, 285.1, and 284.3 eV, which correspond to O=C–O,

C=O, C–O, and C–C/C=C bonds, respectively.[27] In Figure 1d, two pairs major peaks, Fe $2p_{3/2}$ and Fe $2p_{1/2}$, are deconvolved to correspond the elements of Fe^{2+} at 710.5, 723.9eV peaks and Fe^{3+} at 713.9 and 727.4eV peaks. [28-30]

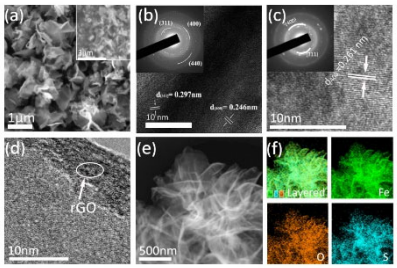

Figure 2 Structural characterization of the pure Fe_3S_4NSs and Fe_3S_4NSs@rGO composites. (a) SEM images of the Fe_3S_4NSs and inside Fe_3S_4NSs@rGO composites. (b) HRTEM images of the pure Fe_3S_4NSs with inside SAED. (c) HRTEM image of the Fe_3S_4NSs@rGO. (Inset: SAED pattern) (d-e) TEM images of Fe_3S_4NSs@rGO. (f) EDS mapping of the Fe_3S_4NSs@rGO.

The size and morphology of Fe_3S_4NSs and Fe_3S_4NSs@rGO were analyzed by SEM, TEM, HRTEM, and mapping images (Figure 2). As shown in Figure 2a, both the Fe_3S_4NSs and Fe_3S_4NSs@rGO exhibit the same 2D ultra-thin nanosheet morphology. The nanosheet structures with a large surface area provide sufficient contact area with electrolyte and reaction sites, which can shorten the diffusion path of sodium ions. [31] SEM images show that Fe_3S_4NSs@rGO has smaller particle size compared to pure Fe_3S_4NSs, comfirming that the rGO controls the size of the nanosheet by suppressing excessive growth of the structure due to the interaction between the matrix of Fe_3S_4 which can be contributed to the reduction of GO. [28, 32] Figure 2b indexes the (311), (400), and (440) planes of the Fe_3S_4 via the selected area electron diffraction (SAED) pattern and provides the same diffraction pattern in HRTEM by measuring the distance d=0.297 nm of (311) plane and the d=0.246 nm of (400) plane. Figure 2c also illustrates the same plane of the greigite Fe_3S_4 in SAED pattern, but the distance (d=0.261nm) in the (400) plane of the Fe_3S_4NSs@rGO was extended compared with the existing 0.246 nm which can boost the sodium insertion kinetics. The presence of rGO could be confirmed through Figure 2d. COOH, COH, etc., which are the main functional groups of rGO, are easily coupled with Fe^{2+} ions. In addition, rGO has a strong surface interaction and buffers the volume expansion of Fe_3S_4 during the sodiation/desodiation processes.[33] Figure 2e−f prove that Fe and S elements are uniformly distributed.

In Figure 3a, the Fe_3S_4NSs@rGO is scanned at a wide voltage range of 0−3 V and 0.5mV s^{-1} rate to confirm the CV plot. The same peaks are found in both the first and second cycles. Peaks were found at charge curve in 1.57V and 1.95V. In the discharge curves, 1.52, 0.71, and 0.44V were measured, respectively. The two cycle curves overlapped each other showing that the charging/discharging process maintains a stable curve after the initial cycle. In Figure 3b, the charge/discharge curve of Fe_3S_4NSs@rGO can be confirmed. The Fe_3S_4NSs@rGO exhibits the initial discharge capacity of 1418 mAh g^{-1} and the charge capacity of 914.4 mAh g^{-1} with 64.83 % coulombic efficiency at 1 A g^{-1}. A charge capacity lower than the discharge capacity resulted from Na^+ ions with other irreversible decomposition reactions in the anode in the solid electrolyte interphase (SEI) formation process. [34, 35]

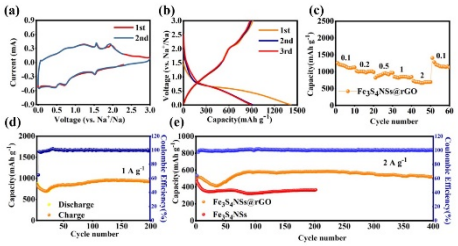

Figure 3. Electrochemical performance of Fe_3S_4NSs@rGO composites compared with pure Fe_3S_4NSs. (a) The CV curves of Fe_3S_4NSs@rGO at scanning rate of 0.5mVs^{-1}. (b) Galvanostatic charge-discharge curve. (c)Rate performance in the voltage range of 0-3V (d) Cycling performance with columbic efficiency at 1A g^{-1}. (e)Cycling data between pure Fe_3S_4NSs and Fe_3S_4NSs@rGO.

In the second and third cycles, discharge capacities of 919 mAh g^{-1} and 899 mAh g^{-1} could be maintained. The rate performance of Fe_3S_4NSs@rGO can be confirmed in Figure 3c. The Fe_3S_4NSs@rGO delivers specific capacities of 1258.7, 1020.9, 821.4, 847.2, and 727.1 mAh g^{-1} at 0.1, 0.2, 0.5, and 1 and 2 A g^{-1} current densities. After that, when it returns to 0.1 A g^{-1} current density, the capacity returns to a high capacity of 1405.8 mAh g^{-1} for excellent rate and reversible performance. To further measure the cycle stability, an attractive capacity of 950 mAh g^{-1} with a stable coulombic efficiency of 100% is obtained at 1 A g^{-1} current density after 200 cycles as shown in Figure 3d. Due to the strong electrical conductivity and mobility of rGO, the electrode's contact resistance decreases, facilitating the rapid removal of electrons. [28] Additionally, the incremental specific capacities in following cycles occur from the formation of a polymeric gel-like coating in the electrode, which is attributed to kinetic activation. [36] Figure 3e shows the long-term cycle performance of Fe_3S_4NSs and Fe_3S_4NSs@rGO at a relatively high current of 2 A g^{-1}. Fe_3S_4NSs shows a capacity of 365.8 mAh g^{-1} after 200 cycles, but Fe_3S_4NSs@rGO shows a capacity twice as high as 524 mAh g^{-1} even after 400 cycles. The increased discharge capacity of Fe_3S_4NSs@rGO is mostly due to the linked rGO network delaying the aggregation of of Fe_3S_4 and reduces the diffusion path for Na-ion shuttling.[23]

4. Conclusion

In summary, Fe_3S_4NSs@rGO was obtained using simple microwave-assist synthesis. The effect of Fe_3S_4NSs@rGO on the structural and electrochemical properties was evaluated compared with the pure Fe_3S_4NSs. Morphological and structural results showed that rGO is successfully composited with Fe_3S_4NSs while maintaining the structure integrity, and the rGO complex is evenly dispersed and doped into the prepared material.

The rGO complex did not cause additional structural deformation and demonstrated that the interaction between the matrixes between Fe_3S_4NSs improves electrical conductivity and the cycle performance of the electrodes. It shows excellent capacities of 1258.7, 1020.9, 821.4, 847.2, and 727.1 mAh g^{-1} at 0.1, 0.2, 0.5, 1, and 2 A g^{-1}. Especially, it maintaines a capacity of 950 mAh g^{-1} even after 200 cycles at 1 A g^{-1} and shows competitive electrochemical performance compared to pure Fe_3S_4NSs.

5. Conflicts of interest

There are no conflicts to declare.

References

1. FENG M, LU Y, YANG Y, et al. Bioinspired greigite magnetic nanocrystals: chemical synthesis and biomedicine applications [J]. Scientific Reports, 2013, 3(1).
2. ROBERTS A P, CHANG L, ROWAN C J, et al. Magnetic properties of sedimentary greigite (Fe3S4): An update [J]. Reviews of Geophysics, 2011, 49(1).
3. WANG X, CAI W, WANG G, et al. One-step fabrication of high performance micro/nanostructured Fe3S4–C magnetic adsorbent with easy recovery and regeneration properties [J]. CrystEngComm, 2013, 15(15).
4. ZHENG J, CAO Y, FU J-R, et al. Facile synthesis of magnetic Fe3S4 nanosheets and their application in lithium-ion storage [J]. Journal of Alloys and Compounds, 2016, 668: 27-32.
5. ARMAND M, AXMANN P, BRESSER D, et al. Lithium-ion batteries – Current state of the art and anticipated developments [J]. Journal of Power Sources, 2020, 479.
6. K. Mizushima, P. C. Jones, P. J. Wiseman, J. B. Goodenough, LixCoO2 A new cathode material for batteries of high energy density [J] Mater. Res. Bull. 1980, 15, 783. [J].
7. Claude Delmas, Jean-Jacques Braconnier, et al. Electrochemical intercalation of sodium in NaxCoO2 bronzes[J]. Solid State Ionics,1981, 3(4): 165-169. [J].
8. LIU T, ZHANG Y, JIANG Z, et al. Exploring competitive features of stationary sodium ion batteries for electrochemical energy storage [J]. Energy & Environmental Science, 2019, 12(5): 1512-33.
9. TAPIA-RUIZ N, ARMSTRONG A R, ALPTEKIN H, et al. 2021 roadmap for sodium-ion batteries [J]. Journal of Physics: Energy, 2021, 3(3).
10. PALOMARES V, CASAS-CABANAS M, CASTILLO-MARTiNEZ E, et al. Update on Na-based battery materials. A growing research path [J]. Energy & Environmental Science, 2013, 6(8).
11. LAN T, MA Q, TSAI C L, et al. Ionic Conductivity of Na3V2P3O12 as a Function of Electrochemical Potential and its Impact on Battery Performance [J]. Batteries & Supercaps, 2020, 4(3): 479-84.
12. ZHOU P, LIU X, WENG J, et al. Synthesis, structure, and electrochemical properties of O′3-type monoclinic NaNi0.8Co0.15Al0.05O2 cathode materials for sodium-ion batteries [J]. Journal of Materials Chemistry A, 2019, 7(2): 657-63.
13. YE L, WANG W, ZHANG B, et al. Regeneration of well-performed anode material for sodium ion battery from waste lithium cobalt oxide via a facile sulfuration process [J]. Materials Today Energy, 2022, 25.
14. MWIZERWA J P, ZHANG Q, HAN F, et al. Sulfur-Embedded FeS2 as a High-Performance Cathode for Room Temperature All-Solid-State Lithium-Sulfur Batteries [J]. ACS Appl Mater Interfaces, 2020, 12(16): 18519-25.
15. SHEN Y, ZHANG Q, WANG Y, et al. A Pyrite Iron Disulfide Cathode with a Copper Current Collector for High-Energy Reversible Magnesium-Ion Storage [J]. Adv Mater, 2021: e2103881.
16. WU J, LIANG Y, BAI P, et al. Microwave-assisted synthesis of pyrite FeS2 microspheres with strong absorption performance [J]. RSC Advances, 2015, 5(80): 65575-82.
17. ZHANG S S. The redox mechanism of FeS2 in non-aqueous electrolytes for lithium and sodium batteries [J]. Journal of Materials Chemistry A, 2015, 3(15): 7689-94.
18. WANG W, LI W, WANG S, et al. Structural design of anode materials for sodium-ion batteries [J]. Journal of Materials Chemistry A, 2018, 6(15): 6183-205.
19. LIU Q, HU Z, ZOU C, et al. Structural engineering of electrode materials to boost high-performance sodium-ion batteries [J]. Cell Reports Physical Science, 2021, 2(9).
20. WANG L, LIU B, ZHU Y, et al. General metal-organic framework-derived strategy to synthesize yolk-shell carbon-encapsulated nickelic spheres for sodium-ion batteries [J]. J Colloid Interface Sci, 2022, 613: 23-34.
21. LI Q, WEI Q, ZUO W, et al. Greigite Fe3S4 as a new anode material for high-performance sodium-ion batteries [J]. Chem Sci, 2017, 8(1): 160-4.
22. WANG Z, ZHANG Y, PENG H, et al. Engineering kinetics-favorable 2D graphene@CuS with long-term cycling stability for rechargeable magnesium batteries [J]. Electrochimica Acta, 2022, 407.
23. KANDULA S, BAE J, CHO J, et al. Gram-scale synthesis of rGO wrapped porous α-Fe2O3 as an advanced anode material for Na-ion batteries with superior cyclic stability [J]. Composites Part B: Engineering, 2021, 220.
24. WU C, ZHENG J, LI J, et al. Fe3S4@reduced graphene oxide composites as novel anode materials for high performance alkaline secondary batteries [J]. Journal of Alloys and Compounds, 2022, 895.

25. FENG C, ZHANG L, YANG M, et al. One-Pot Synthesis of Copper Sulfide Nanowires/Reduced Graphene Oxide Nanocomposites with Excellent Lithium-Storage Properties as Anode Materials for Lithium-Ion Batteries [J]. ACS Appl Mater Interfaces, 2015, 7(29): 15726-34.
26. Hummers, W. S.; Offeman, R. E. Preparation of Graphitic Oxide. J. Am. Chem. Soc. 1958, 80, 1339−1339. [J].
27. LUO J, HU Y, XIAO L, et al. Synthesis of 3D flower-like Fe3S4 microspheres and quasi-sphere Fe3S4-RGO hybrid-architectures with enhanced electromagnetic wave absorption [J]. Nanotechnology, 2019, 31(8): 085708.
28. XU Q-T, LI J-C, XUE H-G, et al. Effective combination of FeS2 microspheres and Fe3S4 microcubes with rGO as anode material for high-capacity and long-cycle lithium-ion batteries [J]. Journal of Power Sources, 2018, 396: 675-82.
29. FU Z, JIANG T, LIU Z, et al. Highly photoactive Ti-doped α-Fe2O3 nanorod arrays photoanode prepared by a hydrothermal method for photoelectrochemical water splitting [J]. Electrochimica Acta, 2014, 129: 358-63.
30. XIA J, JIAO J, DAI B, et al. Facile synthesis of FeS2 nanocrystals and their magnetic and electrochemical properties [J]. RSC Advances, 2013, 3(17).
31. XIE D, CAI S, SUN X, et al. FeS/ZnS nanoflower composites as high performance anode materials for sodium ion batteries [J]. Inorganic Chemistry Communications, 2020, 111.
32. HEIFT D. Iron Sulfide Materials: Catalysts for Electrochemical Hydrogen Evolution [J]. Inorganics, 2019, 7(6).
33. GUO S P, LI J C, XIAO J R, et al. Fe3S4 Nanoparticles Wrapped in an rGO Matrix for Promising Energy Storage: Outstanding Cyclic and Rate Performance [J]. ACS Appl Mater Interfaces, 2017, 9 (43): 37694-701.
34. ZHANG S, LI H, WANG Z, et al. A strongly coupled Au/Fe3O4/GO hybrid material with enhanced nanozyme activity for highly sensitive colorimetric detection, and rapid and efficient removal of Hg(2+) in aqueous solutions [J]. Nanoscale, 2015, 7(18): 8495-502.
35. ZHANG W-M, WU X-L, HU J-S, et al. Carbon Coated Fe3O4Nanospindles as a Superior Anode Material for Lithium-Ion Batteries [J]. Advanced Functional Materials, 2008, 18(24): 3941-6.
36. CABANA J, MONCONDUIT L, LARCHER D, et al. Beyond intercalation-based Li-ion batteries: the state of the art and challenges of electrode materials reacting through conversion reactions [J]. Adv Mater, 2010, 22(35): E170-92.